

# MicroSQUIDs based on V/Cu/V Josephson nanojunctions

Alberto Ronzani,<sup>1,\*</sup> Matthieu Baillegerau,<sup>2</sup> Carles Altimiras,<sup>1</sup> and Francesco Giazotto<sup>1</sup>

<sup>1</sup>*NEST, Istituto Nanoscienze-CNR and Scuola Normale Superiore, I-56127 Pisa, Italy*

<sup>2</sup>*Département de Physique, Ecole Normale Supérieure, 24 Rue Lhomond, F-75005 Paris, France*

We report on the fabrication and characterization of microSQUID devices based on nanoscale vanadium/copper/vanadium Josephson weak links. Magnetically driven quantum interference patterns have been measured for temperatures in the 0.24–2 K range. As magnetometers, these devices obtain flux-to-voltage transfer function values as high as  $450 \mu\text{V}/\Phi_0$  leading to promising magnetic flux resolution  $\Phi_N < 3 \mu\Phi_0/\sqrt{\text{Hz}}$ , being here limited by the room temperature preamplification stage. Significant improvements in the flux noise performance figures, which are already competitive with existing state-of-the-art commercial SQUIDs systems, are expected either with cryogenic preamplification or with the adoption of optimized electronic readout stages based on active feedback schemes.

PACS numbers: 85.25.Dq, 74.45.+c

A superconducting quantum interference device (SQUID) is a magnetic flux sensor constituted by a parallel circuit of two superconducting weak links forming a ring. An external magnetic field threading this loop controls the electron transport properties of the Josephson weak links via flux quantization[1, 2] and the DC Josephson effect[3] therefore modulating the total amount of supercurrent flowing through the circuit. SQUIDs based on low critical temperature superconductors realize extremely sensitive magnetic and current detectors, able to reach nowadays flux noise levels in the  $\sim 0.3\text{--}5 \mu\Phi_0/\sqrt{\text{Hz}}$  range at liquid He temperature[4], with immediate applications in biomagnetism, nuclear magnetic resonance and susceptometry, investigation on the magnetic properties of small spin populations[5, 6], as well as low-noise readout stages for microbolometer detectors[7].

The vast majority of SQUID systems are based on superconductor/insulator/superconductor (SIS) weak links, yet the DC Josephson effect can also be observed in a number of superconducting systems[8], such as constrictions between two superconductor banks[9, 10], or weak links constituted by normal metal[11] or semiconductor elements[12–14]. Superconductor/normal metal/superconductor (SNS) junctions are able to carry a dissipationless phase-dependent supercurrent via the *proximity effect*[15]. The latter induces superconducting correlations in the electronic states of the normal metal when it is placed in good electric contact with a superconductor. Such correlations follow from the building of Andreev bound states in the N region[16–18].

The interest in SNS Josephson junctions is justified by their simple, accessible and reproducible fabrication process. On the one side, the current-phase relation of SNS weak links can be tailored and controlled beyond the conventional sinusoidal shape[19] typical of SIS junctions. This way one can obtain sharper phase respon-

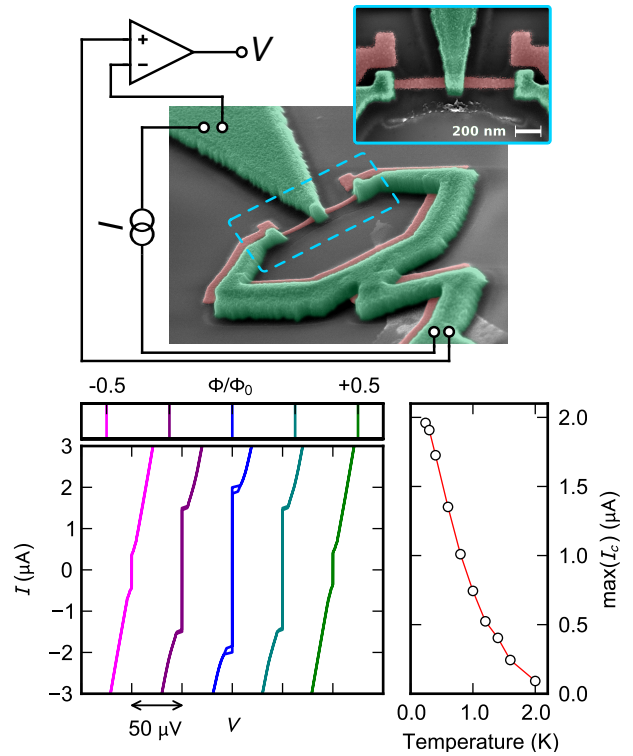


FIG. 1. TOP: Tilted scanning electron micrography showing a typical SQUID device in pseudocolors. Vanadium (green) and copper (red) films are 150 and 20 nm thick, respectively. The standard setup for a four wire measurement is also displayed as a superimposed scheme. The inset in the top right corner shows a perpendicular blow-up of the weak links. BOTTOM LEFT: Current vs voltage ( $I$ - $V$ ) characteristics of device A measured at 240 mK for increasing values of perpendicular magnetic field. The curves have been horizontally offset for clarity. BOTTOM RIGHT: Temperature dependence of the maximum critical current for device A. The line is a guide to the eye.

sivity or have access to non-trivial states such as the  $\pi$ -shifted Josephson junction[20]. On the other side, while

\* [alberto.ronzani@sns.it](mailto:alberto.ronzani@sns.it)

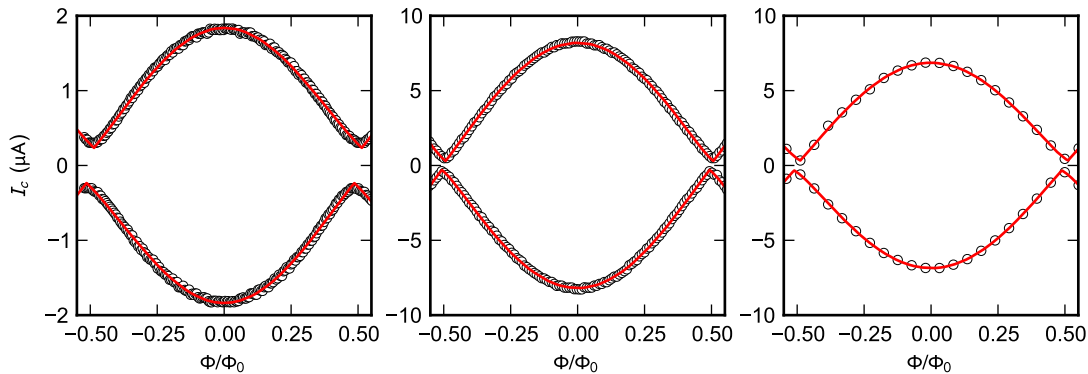


FIG. 2.  $I_c(\Phi)$  dependence for A,B,C devices (left to right). Values for the critical current  $I_c$  have been extracted from the switching current points in the  $I$ - $V$  characteristics measured at 240 mK. Data points (black circles with diameter corresponding to the experimental uncertainty) have been fitted (red line) with the theoretical model displayed in equations (1, 2). Values for the fitting parameters are reported in table I.

SIS Josephson junctions are typically characterized by a considerable capacitance due to the presence of the thin oxide layer of the barrier limiting the performance of SQUIDs[21], SNS Josephson junctions do not suffer from this drawback thanks to their natively negligible capacitance.

A previous work[22] on SQUID magnetometers based on SNS weak links reported devices characterized by critical currents with values of tens of microamperes. However, the usability of these devices was limited by the presence of significant hysteretic behaviour in the voltage-current characteristic curves, a feature typical of high critical current SNS weak links due to heating of the electron gas in the normal domain whenever the junction switches to the resistive state[23].

In order to overcome this issue, we fabricated SQUID devices in which the SNS junctions are somewhat short yet resistive, so that the voltage modulation range (proportional to  $V_{Th} = \hbar D / (eL^2)$ , the Thouless voltage of the normal wire, where  $D$  is the diffusion constant,  $e$  is the electron charge and  $L$  is the length of the wire) is maximized while at the same time the Joule dissipation in the resistive regime is kept as low as possible to quench any thermal hysteresis. The requirement for obtaining resistive SNS junctions can be met via the realization of N wires with nanoscale dimensions.

The top panel of Fig. 1 shows a scanning electron micrograph of a typical interferometer, fabricated by standard electron beam shadow-mask lithography followed by tilted evaporation of Cu/V (20/150 nm) in a UHV chamber. The width and length of copper nanojunctions shown in the inset of the top panel of Fig. 1 are 60 nm and 370 nm, respectively. The loop of the SQUID spans a surface of  $\approx 1.5 \mu\text{m}^2$ . The superconductor of choice, vanadium, shows several attractive features from an applied point of view, such as a sizeable critical temperature ( $T_c \approx 5.4\text{K}$  for thick films) resulting in a strong proximitization capability over copper domains, also made

possible by the good quality of the interfaces formed between these two metals[24].

The electron magneto-transport properties of the SQUIDs were characterized in a filtered  $^3\text{He}$  cryostat having a base temperature of  $\approx 240\text{mK}$ . Current vs voltage characteristics were recorded via lock-in technique by measuring the first harmonic of the voltage response to a DC current bias chopped at a reference frequency ( $f \approx 15\text{Hz}$ ). A 40 dB room temperature low-noise voltage preamplifier (NF Corp. model LI-75A) has been used to boost the signal level to be fed to the digital lock-in amplifier (NF Corp. model LI-5640).

The current vs voltage ( $I$ - $V$ ) characteristics of device A for increasing values of magnetic field applied perpendicularly to the SQUID plane are presented in the bottom left panel of Fig. 1. The characteristic curves show a distinct supercurrent branch; the critical current  $I_c$  being the maximum current that can be sustained in this branch, whose value is modulated by the magnetic field applied to the loop. A small residual hysteresis of thermal origin[23] is present in the characteristics for which the critical current  $|I_c| \gtrsim 1.5 \mu\text{A}$ . As the bias current  $I$  exceeds  $I_c$ , the system switches to a resistive state developing a potential difference across the superconducting loop. For large bias currents,  $I \gg I_c$ , the characteristic curve can be approximated by  $V \approx IR_n/2$ , where  $R_n$  is the normal-state resistance of each weak link. For each known geometry of the copper wire, the measurement of  $R_n$  allows to estimate the diffusion coefficient and, consequently, the Thouless energy ( $E_{Th} = eV_{Th}$ ) of the weak links. Table I summarizes the values of these parameters for the different measured devices. The temperature dependence of the maximum value of the critical current (i.e., that at  $\Phi = 0$ ) for device A is presented in the bottom right panel of Fig. 1. Magnetically modulated supercurrent branches have been measured up to  $\approx 2\text{K}$ .

The  $I$ - $V$  characteristics measured for different values of the applied magnetic flux  $\Phi$  allow the investigation of

Device	$L/W/t$ (nm)	$R_n$ ( $\Omega$ )	$E_{Th}$ ( $\mu\text{eV}$ )	$I_0$ ( $\mu\text{A}$ )	$\alpha_I$	$\beta_{\mathcal{L}}$
A	370/60/20	14.0	27	0.97	0.04	0.14
B	300/150/20	3.6	51	4.10	0.03	0.04
C	280/150/20	3.0	65	3.43	0.06	0.03

TABLE I. Summary of key parameters for all the devices. Length, width and thickness of each N-wire are reported as  $L$ ,  $W$  and  $t$  respectively. The Thouless energy ( $E_{Th} = \hbar D/L^2$ ) has been deduced from the measured normal-state resistance ( $R_n$ ) according to the Einstein relation  $D = (\rho_n \nu_F e^2)^{-1}$ , where  $\rho_n$  is the normal-state resistivity of the N-wire and  $\nu_F = 1.56 \times 10^{47} \text{ J}^{-1} \text{ m}^{-3}$  is the density of states at the Fermi level for copper.  $I_0$ ,  $\alpha_I$  and  $\beta_{\mathcal{L}}$  are parameters from the RSJ model fitted to  $I_c(\Phi)$  experimental data (see Fig. 2).

the functional form  $I_c(\Phi)$  of the magnetic modulation. Data from three different devices (see Fig. 2) have been fitted to the static zero-temperature resistively shunted junction (RSJ) model[25]:

$$i = (1 - \alpha_I) \sin \delta_1 + (1 + \alpha_I) \sin \delta_2 \quad (1a)$$

$$2j = (1 - \alpha_I) \sin \delta_1 - (1 + \alpha_I) \sin \delta_2 \quad (1b)$$

$$\delta_2 - \delta_1 = 2\pi\phi + \pi\beta_{\mathcal{L}}j, \quad (1c)$$

where  $\delta_i$  are the phase differences across the two Josephson junctions,  $\phi = \Phi/\Phi_0$  is the applied magnetic flux normalized to the flux quantum  $\Phi_0 = h/(2e)$ , whereas  $i$  and  $j$  are supercurrent passing through and circulating in the SQUID, respectively. Asymmetries between the two Josephson junctions are accounted for by the introduction of the  $\alpha_I$  parameter. For fixed applied magnetic flux, the positive and negative critical currents ( $I_c^\pm$ ) are defined as proportional to the extremal values of  $i$  over all the values of  $\delta_1$  and  $\delta_2$  that satisfy equations (1) via the coefficient  $I_0$ , representing the magnitude of the maximum supercurrent for each weak link of the SQUID:

$$I_c^+ = I_0 \max_{\delta_1, \delta_2}(i) \quad I_c^- = I_0 \min_{\delta_1, \delta_2}(i). \quad (2)$$

The above model includes also a parametric dependence in equation (1c) on the inductance  $\mathcal{L}$  of the SQUID via the coefficient  $\beta_{\mathcal{L}} = 2\mathcal{L}I_0/\Phi_0$ . Experimental data show excellent agreement with the theoretical model; fitted parameters are summarized in table I. It is worth emphasizing that albeit the RSJ model was developed for SIS Josephson junctions it readily applies also to SNS systems provided that their current-phase relationship is sinusoidal. This is the case for our devices, since they fall in the *long* junction limit, i.e., when the Thouless energy of the junction is much smaller than the superconducting energy gap ( $\Delta_{BCS} \approx 0.8 \text{ meV}$  for bulk vanadium samples).

SQUIDS can be used as magnetometers in the dissipative regime: by biasing the superconducting ring with a constant current exceeding the critical current of the interferometer, changes in magnetic flux can be derived

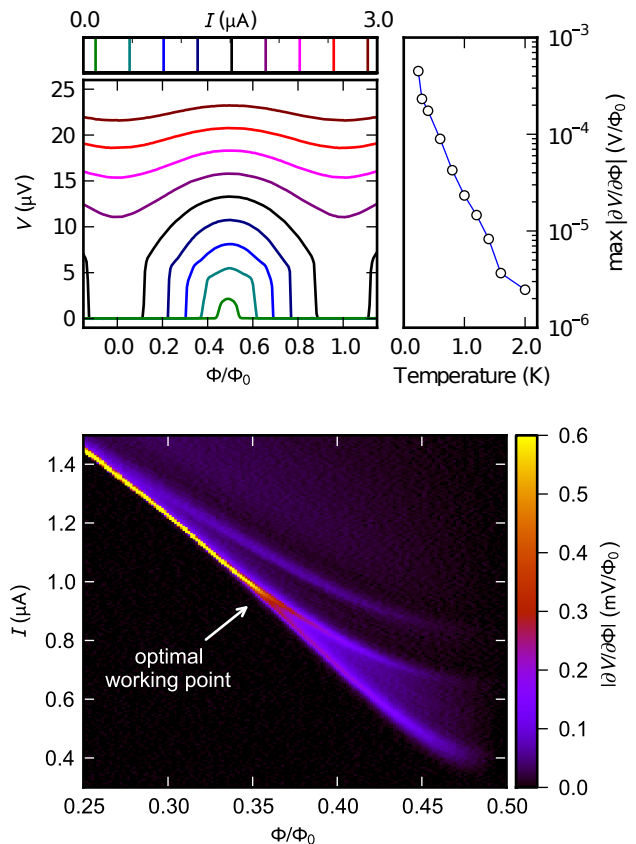


FIG. 3. TOP LEFT: Device A  $V(\Phi)$  characteristics measured at 240 mK for increasing values of current bias  $I$ . TOP RIGHT: Temperature dependence of the maximum stable value of the flux-to-voltage transfer function  $\partial V/\partial\Phi$  for device A. The line is a guide to the eye. BOTTOM: Map of the transfer function of device A obtained by numerical differentiation of  $V(\Phi, I)$  data. The optimal working point for sensitive magnetometry is indicated by a white arrow (see text).

from the corresponding variations in the voltage drop developed across the Josephson junctions.

The  $V(\Phi)$  characteristics of sample A measured at 240 mK are shown in the top left panel of Fig. 3 for different values of the bias current  $I$ . They are periodic in flux with period  $\Phi_0$ , and have an approximate sinusoidal functional form when  $I \gg 2I_0$ . In the opposite limit, the characteristic curves show zero voltage drop  $V$  for magnetic flux values such that  $I < I_c(\Phi)$ , and finite  $V$  values after switching to the dissipative regime in an interval bounded around  $\Phi \approx \Phi_0(n + 1/2)$ , where  $n$  is an integer number. In the switching points themselves the  $V(\Phi)$  characteristics display a strongly non-linear behaviour with high values of the flux-to-voltage transfer function  $|\partial V/\partial\Phi|$  which, in principle, could allow for highly sensitive magnetometry. However, the switching condition cannot be used as a stable working point since the associated dynamic range becomes null as a consequence of the stochastic nature of the switching.

The transfer function has been obtained by numerical

differentiation of the  $V(\Phi, I)$  characteristics measured in high resolution scans of the two-dimensional  $(\Phi, I)$  space. In the resulting map, shown in the bottom panel of Fig. 3, several ridges are evident from the color plot, the most pronounced of which corresponds to the aforementioned switching points. As one moves down to lower values of the bias current  $I$ , the profile of the switching ridge broadens and eventually forks into two different ridges in which the transfer function reaches values approximately equal to  $\approx 0.3 \text{ mV}/\Phi_0$ .

The optimal working point for maximizing sensitivity corresponds to a bias current just above the splitting point for the two ridges. In this point, indicated near the center of the bottom panel of Fig. 3 by a white arrow, the transfer function obtains values as high as  $\approx 0.45 \text{ mV}/\Phi_0$  and is constant over an effective dynamic range of approximately  $10^{-2} \Phi_0$ . The temperature dependence of the maximum (stable) value for the transfer function is reported in the top right panel of Fig. 3, demonstrating the possibility of operation at temperatures up to  $\approx 2 \text{ K}$ , albeit with reduced performance (suppression of approximately one decade per K).

The noise performance of the magnetometers has been characterized by measuring the power spectral density (PSD) of the signal at the output of the preamplifier stage. The magnetic flux resolution of the SQUID is defined as:

$$\Phi_N = \frac{\sqrt{S_v}}{|\partial V/\partial \Phi|_{\text{WP}}}, \quad (3)$$

where  $S_v$  is the noise voltage PSD (in  $\text{V}^2/\text{Hz}$  units) and  $|\partial V/\partial \Phi|_{\text{WP}}$  is the flux-to-voltage transfer function absolute value at the selected working point. Upon setting the SQUID to its optimal working point, the white noise level was detected to be  $\sqrt{S_v} = 1.25 \text{ nV}/\sqrt{\text{Hz}}$  at  $1 \text{ kHz}$ , which is compatible with the input referred noise of the preamplifier; this value corresponds to a magnetic flux resolution  $\Phi_N \approx 2.8 \mu\Phi_0/\sqrt{\text{Hz}}$  at  $1 \text{ kHz}$ .

To test whether the noise limit originates from the preamplification stage itself, two independent battery powered LI-75A units were connected in parallel to the SQUID output. The autocorrelated PSD from one preamplifier and the crosscorrelated spectral density between the two preamplifiers have been extracted and compared. The corresponding magnetic flux resolution spectra are presented in Fig. 4. The autocorrelated spectrum shows the aforementioned  $2.8 \mu\Phi_0/\sqrt{\text{Hz}}$  resolution level, whereas the crosscorrelated one (the blue dashed-dotted line in Fig. 4) reaches a value of  $1.4 \mu\Phi_0/\sqrt{\text{Hz}}$  at  $1 \text{ kHz}$ , thus demonstrating that the magnetic flux resolution for the SQUIDs is here limited by the room-temperature preamplification stage. We stress that the reported magnetic flux sensitivity levels have been measured without the aid of sophisticated electronics or advanced readout schemes, and directly follow from the intrinsic voltage response properties of the SNS weak links.

In summary, we presented the fabrication and characterization of DC microSQUIDs based on V/Cu/V SNS

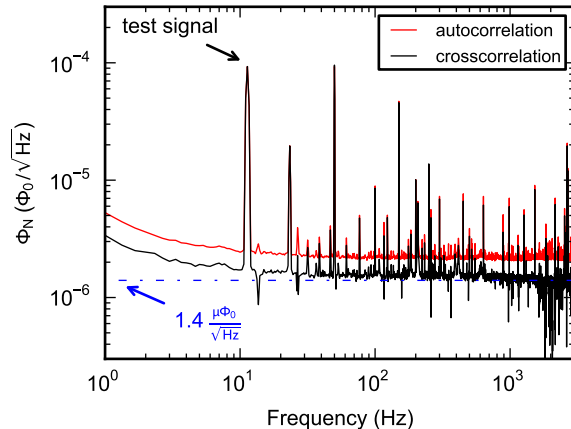


FIG. 4. Magnetic flux resolution characterization for device A measured at  $240 \text{ mK}$  and biased at the optimal working point for maximum sensitivity. Two independent battery-powered preamplifier units were connected in parallel to the SQUID output. The red line represents the flux noise spectrum extracted from the autocorrelation of one preamplifier; the black line represents the crosscorrelated flux noise between the two preamplifier outputs. A small ( $\approx 10^{-4} \Phi_0$ ) applied magnetic flux test signal appears as a peak in the spectra at  $11.7 \text{ Hz}$ .

nanojunctions, which offer technological advantages such as long term stability, reduced aging, as well as fine geometrical control over the transport properties of the Josephson weak links. Magnetic flux resolution figures ( $\Phi_N < 3 \mu\Phi_0/\sqrt{\text{Hz}}$ ), already on par with state-of-the-art commercial DC SQUIDs systems based on SIS technology operating at liquid He temperature, can be further improved by the adoption of advanced SQUID readout techniques[26] such as the addition of passive and active flux feedback schemes and cryogenic preamplification stages. From a more fundamental point of view, the devices herein presented implement three-terminal Andreev interferometers whose non-trivial dynamics emerge reproducibly in their phase-dependent transport properties, here exploited for achieving optimally stable working points for sensitive magnetometry. This phenomenology, not present in conventional SIS systems, is a typical fingerprint of the rich and complex physics underlying the proximity effect[27].

## ACKNOWLEDGMENTS

The authors acknowledge the Italian Ministry of Defense through the PNRM project “TERASUPER”, the Marie Curie Initial Training Action (ITN) Q-NET 264034 for partial financial support. C.A. thanks the Tuscany Region for funding his fellowship via the CNR joint project “PROXMAG”. A.R. thanks Fondazione Tronchetti Provera for funding his Ph.D. scholarship in Scuola Normale Superiore.

- 
- [1] B. Deaver and W. Fairbank, *Physical Review Letters*, 1961, **7**, 43–46.
- [2] R. Doll and M. Näbauer, *Physical Review Letters*, 1961, **7**, 51–52.
- [3] B. Josephson, *Physics Letters*, 1962, **1**, 251–253.
- [4] A. Braginski and Y. Zhang, *The SQUID Handbook vol. 1*, Wiley-VCH Verlag GmbH & Co. KGaA, Weinheim, Germany, 2004, ch. 6, p. 246.
- [5] C. Granata, A. Vettoliere, P. Walke, E. Esposito, C. Nappi, P. Silvestrini, B. Ruggiero and M. Russo, *Journal of Physics: Conference Series*, 2010, **234**, 042010.
- [6] D. L. Tilbrook, *Superconductor Science and Technology*, 2009, **22**, 064003.
- [7] F. Giazotto, T. T. Heikkilä, G. P. Pepe, P. Heliö, A. Luukanen and J. P. Pekola, *Applied Physics Letters*, 2008, **92**, 162507.
- [8] K. Likharev, *Reviews of Modern Physics*, 1979, **51**, 101–159.
- [9] E. M. Levenson-Falk, R. Vijay, N. Antler and I. Siddiqi, *Superconductor Science and Technology*, 2013, **26**, 055015.
- [10] R. Vijay, E. M. Levenson-Falk, D. H. Slichter and I. Siddiqi, *Applied Physics Letters*, 2010, **96**, 223112.
- [11] A. M. Savin, J. P. Pekola, J. T. Flyktman, A. Anthore and F. Giazotto, *Applied Physics Letters*, 2004, **84**, 4179.
- [12] F. Giazotto, P. Spathis, S. Roddaro, S. Biswas, F. Taddei, M. Governale and L. Sorba, *Nature Physics*, 2011, **7**, 857–861.
- [13] F. Carillo, G. Biasiol, D. Frustaglia, F. Giazotto, L. Sorba and F. Beltram, *Physica E: Low-dimensional Systems and Nanostructures*, 2006, **32**, 53–56.
- [14] F. Giazotto, K. Grove-Rasmussen, R. Fazio, F. Beltram, E. H. Linfield and D. A. Ritchie, *Journal of Superconductivity*, 2004, **17**, 317–321.
- [15] B. Pannetier and H. Courtois, *Journal of low temperature physics*, 2000, **118**, 599–615.
- [16] A. Andreev, *Zhurnal Eksperimental'noi i Teoreticheskoi Fiziki, JETP*, 1964, **46**, 1823.
- [17] W. McMillan, *Physical Review*, 1968, **175**, 537–542.
- [18] W. Belzig, F. K. Wilhelm, C. Bruder, G. Schön and A. D. Zaikin, *Superlattices and Microstructures*, 1999, **25**, 1251–1288.
- [19] T. Heikkilä, J. Särkkä and F. Wilhelm, *Physical Review B*, 2002, **66**, 184513.
- [20] J. Baselmans, A. Morpurgo, B. van Wees and T. Klappwijk, *Nature*, 1999, **397**, 1998–2000.
- [21] M. Schmelz, R. Stolz, V. Zakosarenko, T. Schönau, S. Anders, L. Fritzsche, M. Mück, M. Meyer and H.-G. Meyer, *Physica C: Superconductivity*, 2012, **482**, 27–32.
- [22] L. Angers, F. Chiodi, G. Montambaux, M. Ferrier, S. Guéron, H. Bouchiat and J. Cuevas, *Physical Review B*, 2008, **77**, 165408.
- [23] H. Courtois, M. Meschke, J. Peltonen and J. Pekola, *Physical Review Letters*, 2008, **101**, 067002.
- [24] C. P. Garcia and F. Giazotto, *Applied Physics Letters*, 2009, **94**, 132508.
- [25] B. Chesca, R. Kleiner and K. Dieter, *The SQUID Handbook vol. 1*, Wiley-VCH Verlag GmbH & Co. KGaA, Weinheim, Germany, 2004, ch. 2, pp. 30–50.
- [26] D. Drung and M. Muck, *The SQUID Handbook vol. 1*, Wiley-VCH Verlag GmbH & Co. KGaA, Weinheim, Germany, 2004, ch. 4, pp. 127–170.
- [27] J. Cuevas and H. Pothier, *Physical Review B*, 2007, **75**, 174513.